

# Stabilizing edge-fluorination in graphene nanoribbons

Mirco Panighel,<sup>\*,†,⊥</sup> Sabela Quiroga,<sup>‡</sup> Pedro Brandimarte,<sup>¶</sup> Cesar Moreno,<sup>†</sup>  
Aran Garcia-Lekue,<sup>¶,§</sup> Manuel Vilas-Varela,<sup>‡</sup> Dulce Rey,<sup>‡</sup> Guillaume Sauthier,<sup>†</sup>  
Gustavo Ceballos,<sup>†</sup> Diego Peña,<sup>\*,‡</sup> and Aitor Mugarza<sup>\*,†,||</sup>

<sup>†</sup>*Catalan Institute of Nanoscience and Nanotechnology (ICN2), CSIC and The Barcelona Institute of Science and Technology, Campus UAB, Bellaterra, 08193 Barcelona, Spain.*

<sup>‡</sup>*Centro de Investigación en Química Biolóxica e Materiais Moleculares (CiQUS) and Departamento de Química Orgánica, Universidade de Santiago de Compostela. Santiago de Compostela 15782, Spain.*

<sup>¶</sup>*Donostia International Physics Center, Paseo M. de Lardizabal 4, 20018 San Sebastian, Spain.*

<sup>§</sup>*Ikerbasque, Basque Foundation for Science, 48013 Bilbao, Spain.*

<sup>||</sup>*ICREA Institució Catalana de Recerca i Estudis Avançats, Lluís Companys 23, 08010 Barcelona, Spain.*

<sup>⊥</sup>*Current address: CNR-IOM Laboratorio TASC, SS 14 km 163.5 - Basovizza, I-34149 Trieste, Italy.*

E-mail: panighel@iom.cnr.it; diego.pena@usc.es; aitor.mugarza@icn2.cat

## Abstract

The on-surface synthesis of edge-functionalized graphene nanoribbons (GNRs) is challenged by the stability of the functional groups throughout the thermal reaction

steps of the synthetic pathway. Edge-fluorination is a particularly critical case, where the interaction with the catalytic substrate and intermediate products can induce the complete cleavage of the otherwise strong C-F bonds before the formation of the GNR. Here, we demonstrate how a rational design of the precursor can stabilize the functional group, enabling for the first time the synthesis of edge-fluorinated GNRs. The survival of the functionalization is demonstrated by tracking the structural and chemical transformations occurring at each reaction step with complementary X-ray photoelectron spectroscopy and scanning tunneling microscopy measurements. In contrast to previous attempts, we find that the C-F bond survives the cyclodehydrogenation of the intermediate polymers, leaving a thermal window where GNRs withhold more than 80% of the fluorine atoms. We attribute this enhanced stability of the C-F bond to the particular structure of our precursor, which prevents the cleavage of the C-F bond by avoiding interaction with the residual hydrogen originated in the cyclodehydrogenation. This structural protection of the linking bond could be implemented in the synthesis of other  $sp^2$ -functionalized GNRs.

## Abbreviations

CB, CDH, DFT, DOS, GNR, PDOS, RT, STM, VB, XPS

## Keywords

Graphene nanoribbons, on-surface synthesis, edge-functionalization, fluorination, scanning tunneling microscopy, density functional theory, self-assembly

## Introduction

The functionalization of graphene nanoribbons (GNRs) is an effective method for tailoring their structural, chemical and electronic properties.<sup>1-9</sup> Edge functionalization by replacing

hydrogen with different substituents is particularly interesting since it offers a wide flexibility in the choice of functional groups that can, in addition to band tuning,<sup>1</sup> bring chemical selectivity for sensing.<sup>8</sup> Their peripheral position can also be employed to tune inter-ribbon and substrate interactions and drive their organization, one of the most important challenges in bottom-up synthetic methods.<sup>7,10,11</sup> The atomic precision offered by bottom-up synthetic methods in the positioning of each component makes this approach the natural candidate for a controlled functionalization of the ribbons. The thermally activated sequential on-surface synthesis has shown to be particularly effective for the realization of atomically precise GNRs.<sup>12–14</sup> However, such multi-step methods also face a major challenge, namely the stability of the functional groups that have to overcome the whole reaction pathway that leads to the GNR synthesis. This is critical in the functionalization of edges, where the linking groups are not as strongly bound to the aromatic backbone as hetero-atoms in substitutional doping. In the absence of stabilizing intra- or inter-ribbon reactions,<sup>3,6,7</sup> the thermal energy supplied during the synthesis can surpass the linking bond energy, leading to a partial<sup>4</sup> or a total<sup>15</sup> dissociation of the functional groups. Dissociation can occur even in carefully chosen, strongly bonded groups, since the intermediate products formed during the reaction pathway can destabilize the bond between the carbon backbone and the functional group, and induce a premature cleavage. This was recently shown in an attempt to synthesize edge-fluorinated GNRs, where it was found that the activation barrier of the otherwise strong C-F bond was reduced by one order of magnitude, mainly by the formation of an additional C(*sp*<sup>3</sup>)-H bond with residual H migrating from nearest neighbor C atoms during the cyclodehydrogenation (CDH) step.<sup>15</sup> The understanding of this C-F cleaving mechanism can be used for the rational design of fluorinated precursors that avoid the formation of undesired, destabilizing transient structures, as explicitly stated by the authors. Here, we demonstrate how a suitable design of the molecular precursor can lead to the successful synthesis of edge-fluorinated GNRs. These are synthesized on a Au(111) single crystal in a step-wise thermal process, initially via the surface-assisted Ullmann coupling of the fluorinated monomers into poly-

meric chains and then through the subsequent CDH leading to the formation of the graphene nanoribbons.<sup>16</sup> The functionalized precursors have been specifically synthesized to overcome these thermally activated reaction steps. The key element in the design is the separation between the fluorinated carbon and those involved in the CDH reaction, which minimizes the defluorination rate by introducing new paths for residual H release onto the surface. Regarding the electronic properties of the functionalized GNRs, our *ab-initio* calculations reveal a significant n-type doping effect of fluorination, shifting frontier bands downwards by about 200 meV and leaving the size of the gap unchanged. The doping effect, however, can be fully screened out by the interaction with the metallic substrate, as demonstrated by both *ab-initio* and scanning tunneling spectroscopy results.

## Results and discussion

First, we designed a GNR precursor core which could allow us the easy introduction of different functional groups in peripheral positions, with the goal to minimizing the possible group cleavage during the CDH step. With this idea in mind, we selected the benzo[*b*]triphenylene core which is presented in compounds **1a,b** (Figure 1a), including two Br atoms to induce the on-surface Ullmann coupling to form polymers **2a,b** and two phenyl groups to facilitate the CDH step to obtain GNRs **3a,b**. These GNRs resemble the previously reported chevron GNR,<sup>16</sup> although **3a,b** are narrower and characterized by the combination of cove and triple-bay regions along the edges. Besides the unsubstituted GNR **3a** (R = H) we planned to obtain the fluorinated GNR **3b** (R = F). Remarkably, these GNRs were designed with the functional groups attached to remote positions with respect to the carbon atoms involved in the CDH step, in order to minimize the potential weakening and subsequent cleavage of these groups. Precursors **1a,b** were easily obtained by solution chemistry, in three steps from commercially available reagents (Figure 1b). First, bromination of 9,10-phenanthroquinone (**4**) followed by double Knoevenagel condensation with 1,3-diphenylacetone afforded dienone **5** in

good yield. Then, Diels-Alder reaction of **5** with arynes **6a,b** which were *in-situ* generated by fluoride-induced decomposition of triflates **7a,b** led to the formation of benzo[*b*]triphenylenes **1a,b** after CO extrusion of the corresponding adducts.

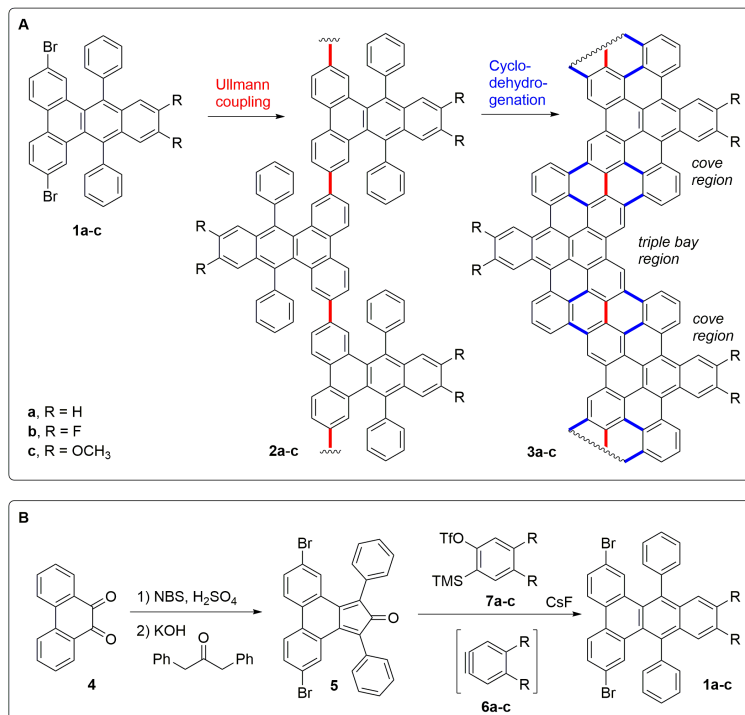


Figure 1: (a) On-surface synthesis of GNRs **3a,b** (b) In-solution synthesis of benzo[*b*]triphenylene derivatives **1a,b** used as GNR precursors.

With compounds **1a,b** in hands, we launched the on-surface studies to attempt the preparation of GNRs **3a,b** on Au(111). The formation of the expected GNRs and the stability of the functional groups throughout the on-surface synthetic protocol have been investigated by complementary scanning tunneling microscopy (STM) and X-ray photoelectron spectroscopy (XPS) measurements. Exploiting the chemical sensitivity of XPS, the reactions resulting in the synthesis of the GNRs have been systematically characterized, as summarized in Figure 2. After depositing compounds **1a,b** at room temperature (RT) and annealing at 200 °C, these GNR precursors undergo a C-Br homolytic bond cleavage, leading to the formation of aryl radicals and the subsequent coupling into polymeric chains **2a,b** via the Ullmann coupling. Figure 2a shows the XPS spectra of the Br 3d core levels for precursor **1b** (R = F).

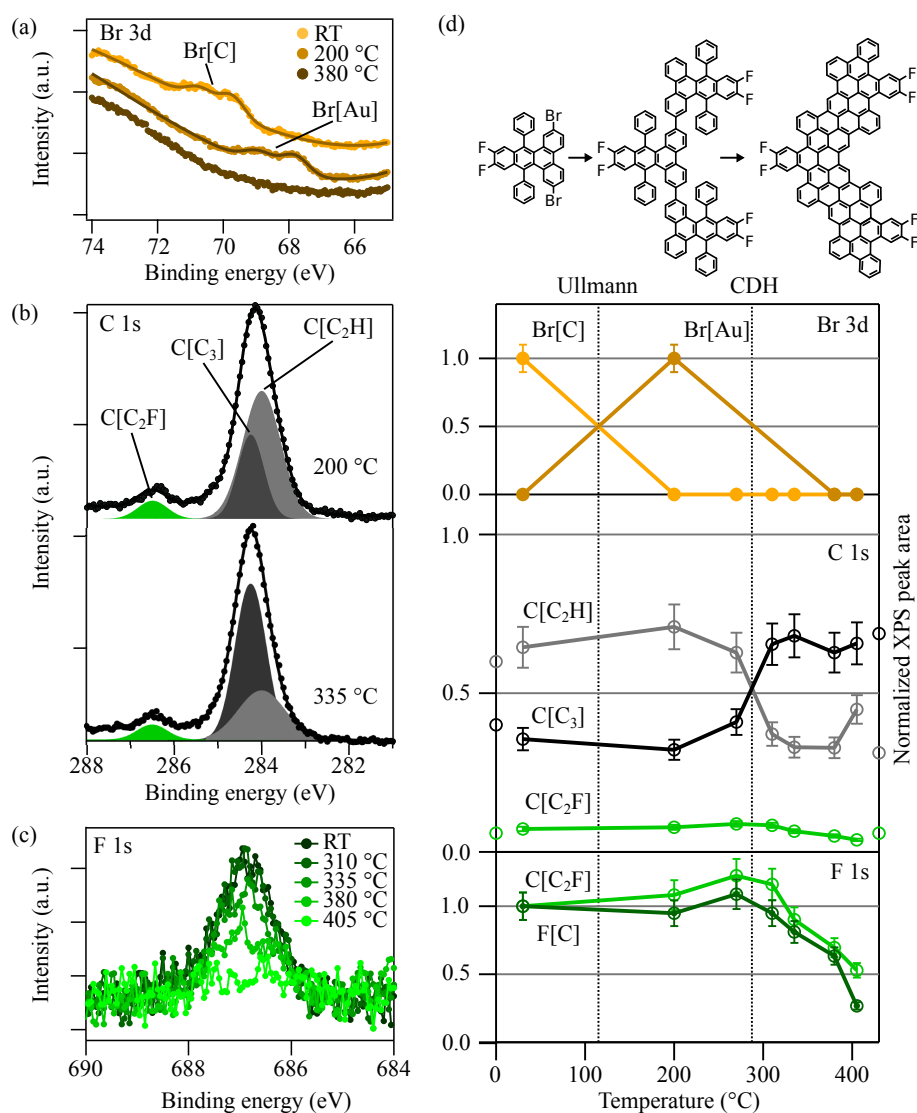


Figure 2: (a)-(c) XPS core level spectra of Br 3d (a), C 1s (b), and F 1s (c) after annealing precursor **1b** at different temperatures. The C 1s spectra fit (continuous lines) is done with multiple peaks to account C[C<sub>3</sub>], C[C<sub>2</sub>H] and C[C<sub>2</sub>F] contributions. (d) Thermal evolution of the XPS atomic ratios, normalized against gold, of the different peaks in (a)-(c). The vertical lines indicate the Ullmann and CDH reaction steps of the GNR synthesis, as indicated by the respective changes in Br[C]/Br[Au] and C[C<sub>3</sub>]/C[C<sub>2</sub>H] ratios. In the C 1s series, the open circles at the left and right limits represent the stoichiometric relation of the different components for the precursors and the nanoribbons respectively. A normalized C[C<sub>2</sub>F] curve has been added to the F[C] data of F 1s.

The binding energy of the spin-orbit split doublet measured for precursors deposited at RT, 69.9/70.9 eV, corresponds to the C-bonded Br. The doublet downshifts by 2.1 eV upon annealing at 200 °C, which can be assigned to C-Br cleavage and consequent formation of Au-bonded Br adsorbates.<sup>17–19</sup> The completion of the C-Br cleavage is in agreement with the Ullmann polymerization observed by STM at the same temperature (see Figure 3). At higher temperature Br adatoms desorb from the surface, as indicated by the absence of any Br 3d peak in the spectrum obtained after annealing at 380 °C. This is clearly visible also in Figure 2d which reports the thermal evolution of the XPS atomic ratios of the different peaks normalized against gold. The CDH reaction that convert polymers **2** into GNRs **3** can be tracked by following the temperature evolution of the C 1s core level components. As representative examples, Figure 2b shows the C 1s core level XPS spectra after annealing **1b** at 200 °C and 335 °C, which illustrate the evolution of C bond ratios that correspond to the CDH step. The main C peak is best fitted with two components that can be assigned to C[C<sub>3</sub>] (284.3 eV) and C[C<sub>2</sub>H] (284.0 eV) bonds respectively. The minor C-Br component is only present at RT according to the Br 3d peak evolution, and therefore is not considered in this analysis. The additional peak present at higher binding energies accounts for the C[C<sub>2</sub>F] (286.5 eV) bond component. As we increase the annealing temperature, a clear inversion of the C[C<sub>3</sub>] and C[C<sub>2</sub>H] components is visible around 300 °C. This is evident in Figure 2d which reports the thermal evolution of the XPS peak area related to the different components. By comparing to the stoichiometric references of the polymeric and GNR phases indicated at the two sides of the graph by open circles, this transition of the C[C<sub>3</sub>]/C[C<sub>2</sub>H] ratio corresponds to the cyclodehydrogenation that leads to the formation of GNRs at this temperature, as also confirmed by the STM measurements (see Figure 3). The relevant features regarding the stability of the functional group are the C[C<sub>2</sub>F] component of C 1s and the correlated F 1s peaks. The evolution of the latter is reported in Figure 2c for the whole set of temperatures investigated. Interestingly, the C[C<sub>2</sub>F] bond survives well above the CDH threshold. As can be seen in detail in Figure 2d, the intensity of the C[C<sub>2</sub>F] components of C 1s and the F[C]

of F 1s remains unaltered during the formation of GNRs at 310 °C, and still withhold 80% of the intensity at 335 °C when the CDH is complete. Their gradual decrease down to about ~25% at the maximum studied temperature of 405 °C is accompanied by an increase of the C[C<sub>2</sub>H] component above the stoichiometric ratio of **3b**, suggesting that cleaved C radicals are passivated by residual H.

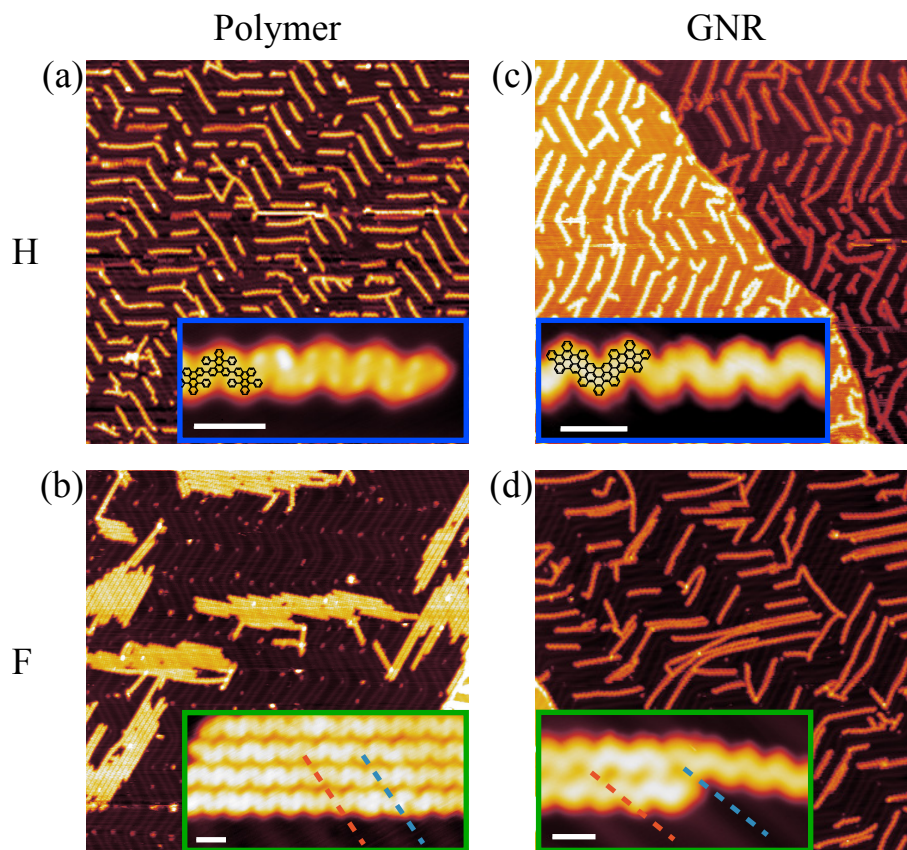


Figure 3: STM images of the polymeric chains and GNRs obtained with the hydrogenated (**1a**) and fluorinated (**1b**) precursors. (a) Polymer **2a** after annealing at 225 °C ( $I_t = 85$  pA,  $V_S = 1.36$  V. Inset:  $I_t = 130$  pA,  $V_S = 1.75$  V). (b) Polymer **2b** after annealing at 225 °C ( $I_t = 46$  pA,  $V_S = 2.52$  V. Inset:  $I_t = 60$  pA,  $V_S = 1.28$  V). (c) GNR **3a** after annealing at 400 °C ( $I_t = 75$  pA,  $V_S = 1.36$  V. Inset:  $I_t = 250$  pA,  $V_S = -0.1$  V). (d) GNR **3b** after annealing at 335 °C ( $I_t = 80$  pA,  $V_S = 1.30$  V. Inset:  $I_t = 210$  pA,  $V_S = 1.23$  V). The surface stacking domains of the Au(111) herringbone reconstruction are marked with red (face-centered cubic, fcc) and cyan (hexagonal closed packed, hcp) dashed lines. Images size is 150x150 nm<sup>2</sup>. All inset scale bars correspond to 2 nm.

We next compare the XPS spectroscopic analysis with the structural information provided by STM at each reaction step. Figure 3 shows representative STM topographic images for



the polymeric chains and GNRs synthesized with precursors **1a** (R = H) and **1b** (R = F). In both cases, annealing at 200 °C leads to the Ullmann polymerization of precursors into chains with a zig-zag backbone of an apparent height of 0.2 nm, and protrusion pairs with a center-to-center distance of 0.8 nm. The comparison of the polymeric unit structure with the precursor monomer confirms that the double protrusions correspond to the out-of-plane phenyl rings and that functional groups stay on the protruding edge of the zig-zag backbone (see insets in Figure 3a,b). Further annealing (at 335 °C for F-GNR and 400 °C for H-GNR) leads to the formation of planar chevron-type structures (insets in Figure 3c,d), as expected from the incorporation of the side phenyl rings into the backbone after the CDH reaction. The overall apparent height of 0.15 nm of this structure is in good agreement with previously reported GNRs.<sup>16,19</sup> Despite their similar intra-molecular structural evolution, the substituents of each precursor leads to inter-molecular interactions that dictate distinct assembly patterns. This is most evident at the intermediate polymeric phase (Figure 3a). In the case of **2a** the interaction with the herringbone reconstructed Au(111) surface guides the polymer assembly. The single chains fill the face-centered cubic (fcc) tracks, terminating at the kinks of the herringbone zigzag, and hence giving rise to a superlattice of chains with a narrow length distribution that is determined by the zigzag period. In contrast, F-mediated inter-chain interactions for **2b** are strong enough to bunch them in parallel arrays that appear off-registry with the herringbone template, avoiding any size restriction imposed by it. The differences are minimized after the aromatization of the polymers into GNRs (Figure 3b). In this step, GNR **3a** simply replicates the polymer superlattice, whereas the stronger interaction of the planar structures with the substrate causes a debunching of **2b** arrays into single **3b** GNRs that now try to follow the herringbone reconstruction. The overgrown GNRs, however, do not fit in the zigzag units of the reconstruction and consequently the quality of the superlattice is significantly reduced. The stability of **3b**, the chevron-type fluorinated GNR synthesized in this work, is in contrast to previous attempts of synthesizing edge-fluorinated armchair GNRs using different anthracene derivatives as precursors.<sup>15,20</sup> In these

cases polymers were fully defluorinated before turning into GNRs. With the C-F bond being one of the strongest C-heteroatom single bond, the premature cleavage was unexpected and attributed to a combination of surface and byproduct assisted bond weakening. According to the density functional theory (DFT) calculations,<sup>15</sup> the interaction with the underlying Au atoms already reduces the activation energy of the C( $sp^2$ )-F bond cleavage by 100 kJ/mol. A more significant weakening is induced by the  $sp^3$  bonding of a residual H generated in the nearest neighbor C atom during the CDH, which brings the activation energy further down by 400 kJ/mol. Altogether, the two effects reduce the C-F cleavage activation energy close to an order of magnitude, from ~540 kJ/mol to ~40 kJ/mol.

We studied the C-F bond stability of **3b** by performing gas-phase DFT calculations (see Figure 4), leading to similar conclusions as for the armchair fluorinated GNRs of Ref. 15. The C( $sp^3$ )-H bond formation leads to a similar reduction of ~400 kJ/mol of the C-F bond cleavage activation energy, from 554 kJ/mol in C( $sp^2$ )-F to 152 kJ/mol in H-C( $sp^3$ )-F, indicating that the local environment is the most important factor determining the stability of these bonds. We also find that for H-C( $sp^3$ )-F, defluorination is favorable over dehydrogenation by ~75 kJ/mol. The main conclusion of the above analysis is that the C-F bond in the H-C( $sp^3$ )-F group is not more stable in the chevron GNRs of the present work than in the armchair GNRs described in Ref. 15. The difference between the two cases lies in the probability of obtaining the transient H-C( $sp^3$ )-F configuration. Since migration barriers are expected to be similar for different ribbon topologies, the formation rate of the H-C( $sp^3$ )-F group will mainly depend on the specific sites where residual H are originated during the CDH reaction with respect to the fluorinated C position. For the armchair GNRs described in Ref. 15, H is released from the vicinal C atom, and a low migration energy barrier of ~80 kJ/mol to the fluorinated C atom results in a high formation rate of the transient H-C( $sp^3$ )-F configuration ( $k \sim 10^7 \text{ s}^{-1}$  at 400 °C). In contrast, the particular design of our precursor relocates the closest formation of residual H significantly further away, at the 5<sup>th</sup> nearest neighbor (see Figure 4b and path 1 in Figure 4c). This introduces new low acti-

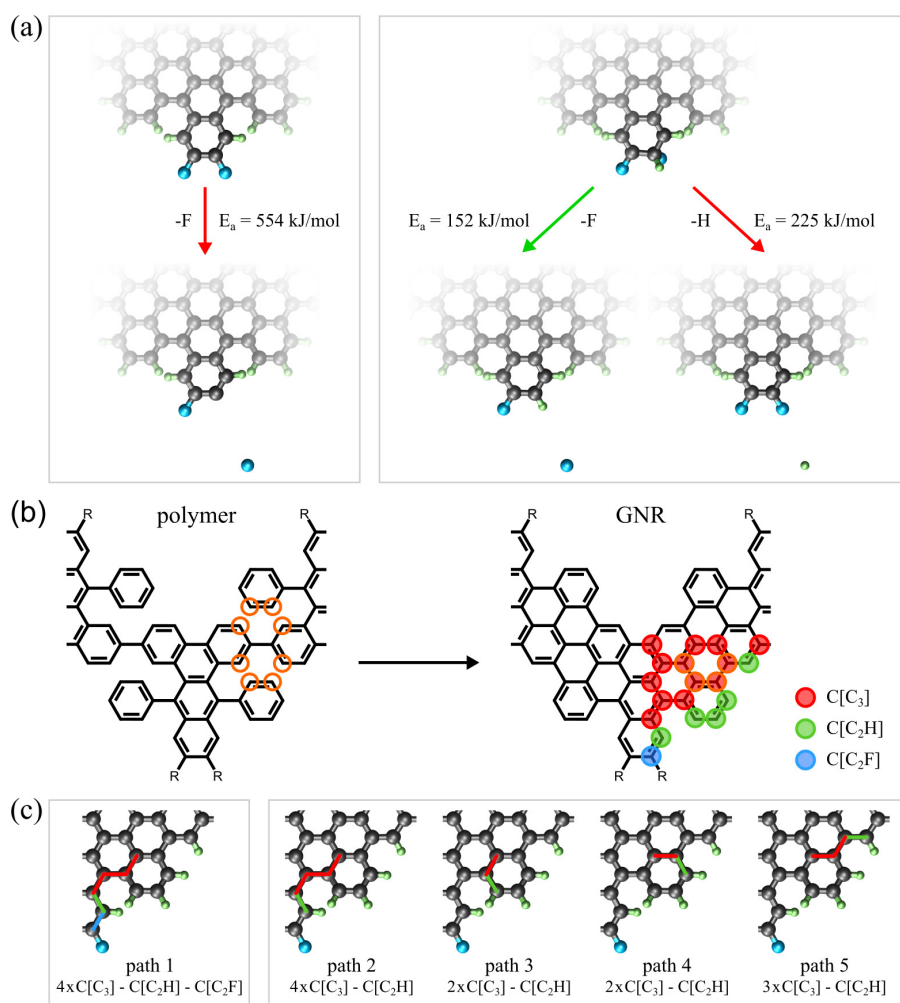


Figure 4: Stability analysis of the C-F bond. (a) Calculated dissociation energies of the  $\text{C}(\text{sp}^2)\text{-F}$  bond (left) and of C-H and C-F bonds within the  $\text{H-C}(\text{sp}^3)\text{-F}$  group during the formation of GNR **3b**. (b) The three different families of  $\text{C}(\text{sp}^2)$  atoms depending on their local environment in the GNR sub-unit. (c) Possible migration paths of the closest H atom towards the edge C, marked with the color code of the families in b.

vation barrier paths for the release of the residual H into the surface via the hydrogenated C edge atoms, effectively preventing the formation of the  $\text{H-C}(sp^3)\text{-F}$  groups and therefore the corresponding defluorination. In our analysis of H release paths, we only consider residual H generation closest to the C-F bond, noting that the others only differ by additional migration steps within the GNR backbone. This originates from the cleavage of the C-H pair marked in orange circles in the polymer of Figure 4b. Each pair produces one  $\text{C}(sp^3)\text{-H}$  after the C-C coupling, since the C-H pointing downwards is directly released to the surface.<sup>15,21</sup> In total, we find 5 possible paths from this initial position of the residual H to the nearest C edge atoms, which are sketched in Figure 4c. The color of the segments in each path indicates hopping to three different carbon types,  $\text{C}[\text{C}_3]$ ,  $\text{C}[\text{C}_2\text{H}]$  and  $\text{C}[\text{C}_2\text{F}]$ , corresponding to fully carbon-bonded, hydrogenated and fluorinated edge atoms respectively (see Figure 4b). Path 1 is the one inducing defluorination by the mechanism proposed in Ref. 15, whereas paths 2-5 reach hydrogenated edge C atoms that can release the residual H to the surface by an equivalent dehydrogenation process.<sup>21</sup> A common property shared by both fluorinated and hydrogenated edges is that, in the presence of a  $\text{C}(sp^3)\text{-H}$  bond, they are both characterized by an activation energy for C-F and C-H bond cleavage that is significantly smaller than the migration barrier of the residual H to the vicinal C.<sup>15,21</sup> The probability ratio between C-F and C-H cleavage will then exclusively depend on the probability of arrival of the residual H to the corresponding edge C atom. This is effectively reduced by the topology of **3b** in two ways: providing multiple additional paths for H release (paths 2-5) and, more importantly, interposing one of these paths (path 2) to the defluorination one (path 1). Altogether, the precursor design effectively prevents defluorination during the synthesis, as demonstrated directly by the temperature dependent XPS measurements.

Some effects of fluorination are imprinted in the electronic properties, despite the apparent low density of edge fluorination exhibited by GNR **3b**. DFT calculations of the gas-phase structure reveal a significant downshift of valence and conduction bands of  $\sim 200$  meV (see Figure 5a), which can be seen as an electrostatic n-gating induced by the electron accu-

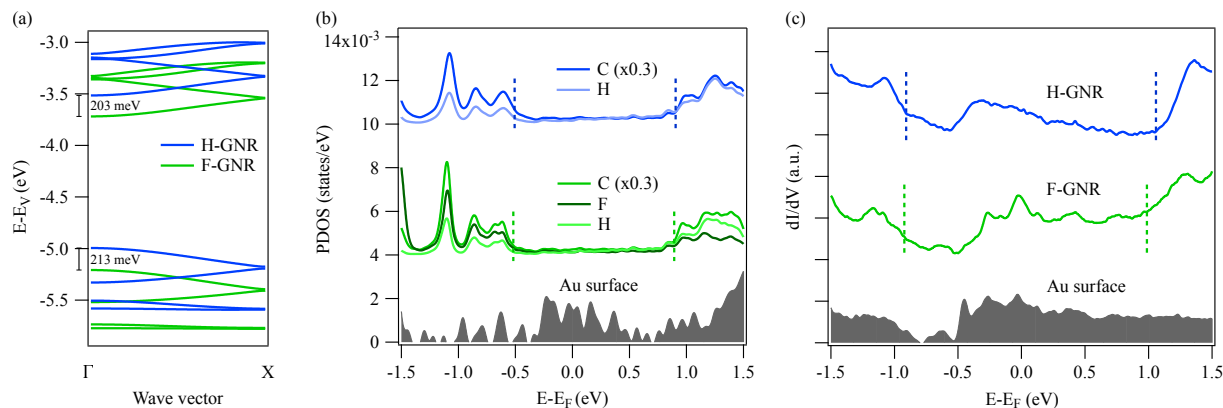


Figure 5: Electronic structure of the GNRs **3a**, **b**. (a) Band structures of free-standing **3a** (H-GNR, blue) and **3b** (F-GNR, green) for the structures relaxed on Au(111). Energies given with respect to the vacuum energy. (b) PDOS on the different chemical species from **3a** (blue curves, top) and from **3b** (green curves, middle), both calculated on a Au(111) substrate and with a Lorentzian broadening of 35 meV. The PDOS on the surface Au atoms far from the GNR is shown in shaded gray at the bottom (see Methods). (c) Representative constant-height dI/dV spectra taken on **3a** (after CDH at 400 °C) and **3b** (after CDH at 335 °C) in the position of the functional group. Spectrum taken on clean Au is reported in shaded gray as reference.

mulation at the fluorine atoms. As opposed to fully edge-halogenated armchair<sup>1</sup> and cove<sup>2</sup> GNRs, the size of the band gap is barely affected by the fluorination (1.48/1.49 eV for **3a**/**3b** respectively), probably due to the lower nominal density of edge-fluorination and different topology of our chevron GNRs. Indeed, a similar quasi-rigid downshift have been also observed in N-doped chevron GNRs.<sup>22,23</sup> The band shift, however, is reduced to negligible values ( $\sim 10$  meV) when GNRs interact with the Au substrate, as can be noted from the projected density of states (PDOS) plotted in Figure 5b. We attribute this band realignment to interfacial charge redistribution, similar to that leading to the Fermi level pinning observed in armchair GNRs.<sup>24</sup> An additional effect of the surface is the reduction of the band gap from  $\sim 1.5$  eV to 1.3 eV for free-standing and on-Au GNRs respectively, which is attributed to hybridization with Au states. The absence of any sizeable band gap difference and shift is reproduced in comparative spectroscopic measurements performed in **3a** and **3b** GNRs on the Au substrate (see Figure 5c). Here we find the onset of the valence band (VB) fixed at  $-0.91$  eV for both GNRs, whereas the onset of the conduction band (CB) can be identified

1  
2  
3 at 1.05 eV for **3a** and 0.95 eV for **3b**. The resulting gaps of 1.96 eV and 1.86 eV are slightly  
4  
5 larger than the 1.3 eV obtained by DFT, which is accounted by the well-known gap under-  
6  
7 estimation of this method.<sup>25</sup> According to the PDOS analysis of Figure 5b, the bands with  
8  
9 significant fluorine spectral contribution produces PDOS maxima at around 1 eV below the  
10  
11 VB, which referred to the experimental spectra would corresponds to a bias voltage of -2 eV.  
12  
13 Unfortunately, the **3b** GNRs were not stable at this large bias voltage, probably due to tip-  
14  
15 induced C-F bond cleavage, hindering the detection of any direct spectroscopic fingerprint  
16  
17 of the fluorine atoms.  
18  
19

## 20 21 Conclusion

22  
23 We have demonstrated the on-surface synthesis of edge-fluorinated GNRs. Our combined  
24  
25 thermal evolution study of XPS and STM measurements provides chemical and structural  
26  
27 evidences of the formation of chevron type GNRs and the survival of fluorine functionaliza-  
28  
29 tion throughout the whole synthetic path. As opposed to the case of armchair type GNRs  
30  
31 based on fluorinated anthracene derivatives (DBTA), where the polymers are fully deflu-  
32  
33 orinated before the formation of GNRs, we achieve 100% of fluorination at the threshold  
34  
35 of GNR formation. In a thermal window of 40 °C above that threshold we only observe a  
36  
37 slight decrease to 80%. According to first-principle calculations, the electronegative fluorine  
38  
39 atoms tend to shift the valence and conduction bands of free-standing GNRs to lower bind-  
40  
41 ing energies by about 200 meV without affecting the size of the gap. However, this shift is  
42  
43 canceled out in the experimental dI/dV spectra due to the pinning effect of the underlying  
44  
45 metallic substrate. The stability of the fluorine substituents is attributed to the particular  
46  
47 design of the precursor, in which the F atoms are introduced in remote positions with respect  
48  
49 to the cyclodehydrogenation regions. By providing alternative H release paths, our design  
50  
51 effectively hampers the migration of residual H originated during cyclodehydrogenation to  
52  
53 the fluorinated C edge atom, and the consequent formation of the H-C(*sp*<sup>3</sup>)-F bond that  
54  
55 facilitates the C-F bond cleavage. These alternative H release pathways are independent of  
56  
57  
58  
59  
60

the functional group, and hence we expect that our approach should enable the synthesis of other edge-functionalized GNRs. The structural origin of the stabilization highlights the relevance of a rational design of precursors not only for achieving a particular topology of the final product but also for defining reaction pathways that avoid destabilizing transient structures.

## Methods

STM and XPS measurements were performed in two separated ultra-high vacuum (UHV) systems with a base pressure below  $5 \times 10^{-10}$  mbar. Clean Au(111) samples were prepared by cycles of Ar ion sputtering at 1 keV and annealing at 470 °C for 20 minutes. Surface cleanliness has been checked by low energy electron diffraction (LEED) and either STM or XPS. Molecular precursors have been deposited from a resistively heated crucible on the Au(111) substrate kept at RT. For the sub-monolayer coverage studied, **1a** and **1b** were sublimated at 280 °C and 300 °C respectively. The sample was annealed at a rate of about 1 K/s and kept 15 minutes at the indicated temperatures to promote the polymerization and cyclodehydrogenation reactions. Sample temperatures were measured with an infrared pyrometer in the XPS setup and a thermocouple directly spot-welded on the sample holder in the STM setup. The pyrometer was previously calibrated with the sample holder thermocouple of the STM setup in order to have reliable temperature comparison between the two measuring methods. STM measurements have been carried out with a Createc LT-STM operated at samples temperatures of 5 K, except for the image of the inset of Figure 3c, which was acquired at 77 K. STM topographic images have been acquired in constant-current mode and analyzed and processed with Gwyddion software.<sup>26</sup> STM dI/dV spectra have been measured at 5 K in constant-height mode with the lock-in technique and a bias modulation of 20 mV. Due to the difficulty of determining the VB/CB maxima/minima in the broad experimental features, both the theoretical and experimental band gaps have been determined by consid-

1  
2  
3 ering the onset of the corresponding features. This represents a lower limit in the estimation  
4 of the band gaps. XPS measurements were carried out at RT with a SPECS Phoibos 150  
5 hemispherical energy analyzer using a monochromatic Al K $\alpha$  X-ray source at 1486.6 eV.  
6 XPS spectra have been referenced to the Fermi level, fitted with a Fermi-Dirac distribution  
7 at the sample temperature.  
8  
9  
10  
11  
12

13 First-principles calculations were performed via Density Functional Theory as imple-  
14 mented in the SIESTA package.<sup>27,28</sup> Here the valence electrons are described with a basis  
15 set given by a linear combination of numerical atomic-orbitals, in our case a double- $\zeta$  plus  
16 polarization (DZP) basis set with the orbital radii defined using a 50 meV energy shift.<sup>28</sup> We  
17 adopted for the top Au atomic layer an extended DZP basis optimized for the description of  
18 the Au(111) surface<sup>29</sup> as well as a Hydrogen passivation of the slab bottom layer to prevent  
19 spurious effects due to the proximity of the surface states on the slab representation.<sup>30</sup> More-  
20 over, for a better description of the carbon states, the basis set was extended to included 3s  
21 and 3p orbitals.<sup>6</sup> The core electrons were represented by norm-conserving Troullier-Martins  
22 pseudopotentials.<sup>31</sup> Dispersive interactions were considered via the van der Waals density  
23 functional by Dion et al<sup>32</sup> with the modified exchange by Klimeš, Bowler and Michaelides.<sup>33</sup>  
24 The fineness of the grid for integrations in real space was defined using a 300 Ry energy cut-  
25 off. The self-consistency cycle was stopped when the changes of the density matrix elements  
26 were less than  $10^{-5}$  and also lower than  $10^{-4}$  eV for the Hamiltonian matrix elements. The  
27 smearing of the electronic occupations was defined by an electronic temperature of 300 K  
28 with a Fermi-Dirac distribution. The structures were allowed to fully relax until the forces  
29 were lower than 10 meV/Å on top of a 3-layer thick slab within a 17.65x30.57x60 Å<sup>3</sup> sim-  
30 ulation cell (with the two bottom layers kept fix with experimental lattice). We used a 15  
31 k-point mesh along the GNRs periodic direction (x) and for calculations involving the Au  
32 substrate 3 k-points were adopted along the other periodic direction (y) as well. The Au  
33 surface density of states (DOS), shown in Figure 5b, was obtained by the difference between  
34 the DOS projected on the Au atoms in the surface layer and far from the GNR and the DOS  
35  
36  
37  
38  
39  
40  
41  
42  
43  
44  
45  
46  
47  
48  
49  
50  
51  
52  
53  
54  
55  
56  
57  
58  
59  
60



projected on the Au atoms in middle slab layer, which has been shown to provide a good estimation using similar parameters.<sup>34</sup>

## Acknowledgement

We are indebted to D. Pérez and E. Guitián for fruitful discussions. C.M. was supported by the Agency for Management of University and Research grants (AGAUR) of the Catalan government through the FP7 framework program of the European Commission under Marie Curie COFUND action 600385 funded by the CERCA Program/Generalitat de Catalunya. We acknowledge support from the Spanish Ministry of Economy and Competitiveness, MINECO (under Contracts No. MAT2016-78293-C6, FIS2017-83780-P and Severo Ochoa No. SEV-2017-0706), the European Regional Development Fund (ERDF), the Interreg V-A España-Francia-Andorra program (Contract No. EFA 194/16 TNSI), the EU project SPRING (863098), the Xunta de Galicia (Centro singular de investigación de Galicia accreditation 2016-2019, ED431G/09).

## Supporting Information Available

### Molecular synthesis

#### General aspects

All reactions were carried out under argon using oven-dried glassware. THF, CH<sub>2</sub>Cl<sub>2</sub>, and CH<sub>3</sub>CN were purified by a MBraun SPS-800 Solvent Purification System. Finely powdered CsF was dried under vacuum at 100 °C, cooled under argon and stored in a glove-box. TLC was performed on Merck silica gel 60 F254; chromatograms were visualized with UV light (254 nm and 360 nm). Flash column chromatography was performed on Merck silica gel 60 (ASTM 230-400 mesh). <sup>1</sup>H and <sup>13</sup>C NMR spectra were recorded at 300 and 75 MHz or 500 and 126 MHz (Varian Mercury 300, Bruker AMX-500 instruments, respectively). Low-resolution electron impact mass spectra were determined at 70 eV on a HP-5988A instrument. High-resolution mass spectra (HRMS) were obtained on a Bruker Microtof spectrometer.

Commercial reagents were purchased from ABCR GmbH or Aldrich Chemical Co. and were used without further purification. Molecules **5** and **7a-b** were prepared following published procedures (Figure S1)<sup>1</sup>.

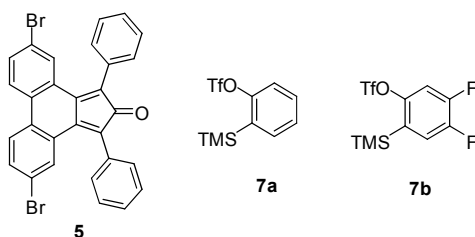
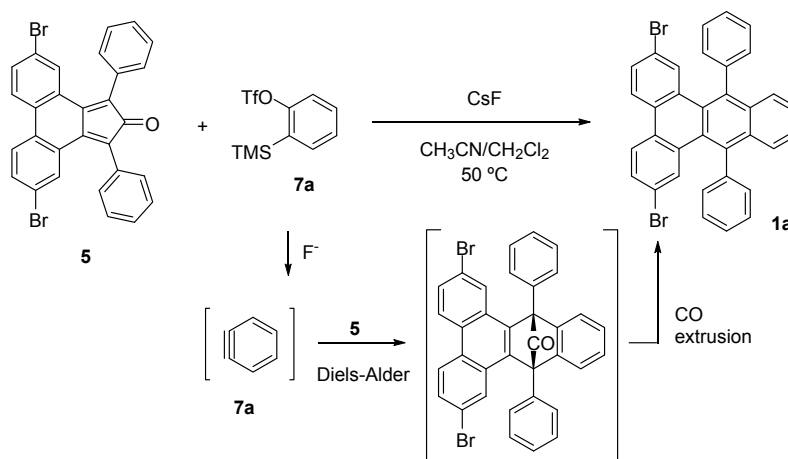


Figure 6: Structures of starting materials **5** and **7a-b**.

Figure 7: Synthesis of compound **1a**.

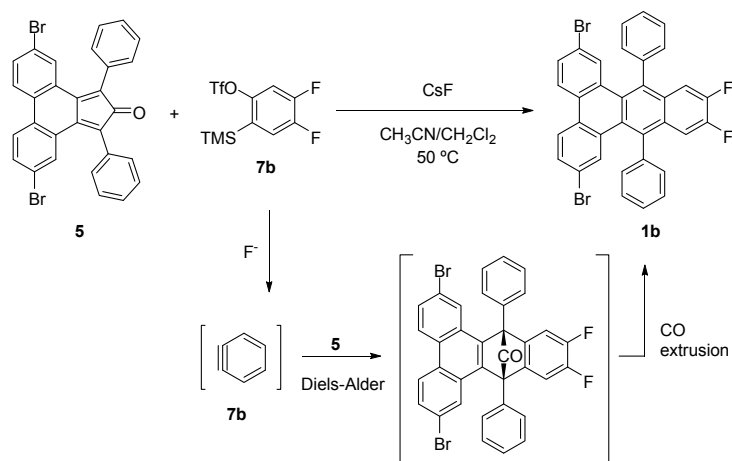
### Synthesis of 2,7-dibromo-9,14-diphenylbenzo[f]tetraphene (**1a**)

Finely powdered anhydrous CsF (170 mg, 1.09 mmol) was added over a solution of dienone **5** (125 mg, 0.24 mmol) and triflate **7a** (110 mg, 0.36 mmol) in CH<sub>3</sub>CN/CH<sub>2</sub>Cl<sub>2</sub> (1:1, 6 mL). The mixture was heated at 50 °C under argon for 16 h. Then, the solvent was evaporated under reduced pressure and the residue was purified by column chromatography (SiO<sub>2</sub>; hexane/CH<sub>2</sub>Cl<sub>2</sub> 4:1) to isolate compound **1a** (87 mg, 61%) as a yellow solid. <sup>1</sup>H NMR (300 MHz, CDCl<sub>3</sub>) δ: 8.05 (d, *J* = 8.6 Hz, 2H), 7.95 (dd, *J* = 6.6, 3.3 Hz, 2H), 7.61 – 7.50 (m, 12H), 7.48 (d, *J* = 3.3 Hz, 2H), 7.43 (dd, *J* = 8.6, 1.9 Hz, 2H) ppm. <sup>13</sup>C NMR (125 MHz, CDCl<sub>3</sub>) δ: 141.2 (2C), 136.6 (2C), 133.6 (2CH), 133.2 (2C), 132.7 (2C), 132.5 (4CH), 130.1 (2CH), 129.5 (4CH), 129.2 (2C), 128.3 (2CH), 127.7 (2C), 127.1 (2CH), 126.5 (2CH), 124.7 (2CH), 120.6 (2C) ppm. MS (EI), *m/z* (%): 588 (M<sup>+</sup>, 100), 508 (14), 428 (15), 350 (20), 212 (16). HRMS (EI) for C<sub>34</sub>H<sub>20</sub>Br<sub>2</sub>, calculated: 585.9932, found: 585.9949.

### Synthesis of 2,7-dibromo-11,12-difluoro-9,14-diphenylbenzo[f]tetraphene (**1b**)

Finely powdered anhydrous CsF (198 mg, 1.31 mmol) was added over a solution of dienone **5** (150 mg, 0.29 mmol) and triflate **7b** (136 mg, 0.41 mmol) in CH<sub>3</sub>CN/CH<sub>2</sub>Cl<sub>2</sub> (1:1, 24

<sup>1</sup>a) For synthesis of dienone **5**, see: Vo, T. H.; Shekhirev, M.; Kunkel, D. A.; Morton, M. D.; Berglund, E.; Kong, L.; Wilson, P. M.; Dowben, P. A.; Enders, A.; Sinitskii, A. Nat. Commun. 2014, 5, 3189. b) For preparation triflates **7a-b**, see: Peña, D.; Cobas, A.; Pérez, D.; Guitián, E. Synthesis 2002, 1454.

Figure 8: Synthesis of compound **1b**.

mL). The mixture was heated at 50 °C under argon for 16 h. Then, the solvent was evaporated under reduced pressure and the residue was purified by column chromatography (SiO<sub>2</sub>; hexane/CH<sub>2</sub>Cl<sub>2</sub> 4:1) to isolate compound **1b** (72 mg, 40%) as a pale yellow solid. <sup>1</sup>H NMR (353 K, 500 MHz, C<sub>2</sub>D<sub>2</sub>Cl<sub>4</sub>) δ: 8.02 (d, *J* = 8.6 Hz, 2H), 7.64 – 7.52 (m, 10H), 7.49 – 7.39 (m, 6H) ppm. <sup>13</sup>C NMR (353 K, 126 MHz, C<sub>2</sub>D<sub>2</sub>Cl<sub>2</sub>) δ: 150.43 (dd, *J* = 253.4, 17.7 Hz, 2CF), 140.74 (2C), 136.18 (2C), 133.51 (2CH), 132.65 (2C), 132.06 (4CH), 130.49 (2CH), 130.44 (2C), 130.22 (4CH), 129.87 (2CH), 128.81 (2C), 128.38 (4CH), 124.80 (2C), 120.76 (2C), 113.19 (dd, *J* = 13.7, 6.6 Hz, 2CH) ppm. MS (EI), *m/z* (%): 623 (100), 543 (24). HRMS (APCI (M+1)) for C<sub>34</sub>H<sub>18</sub>Br<sub>2</sub>F<sub>2</sub>, calculated: 621.9738, found: 621.9730.

### <sup>1</sup>H and <sup>13</sup>C NMR spectra

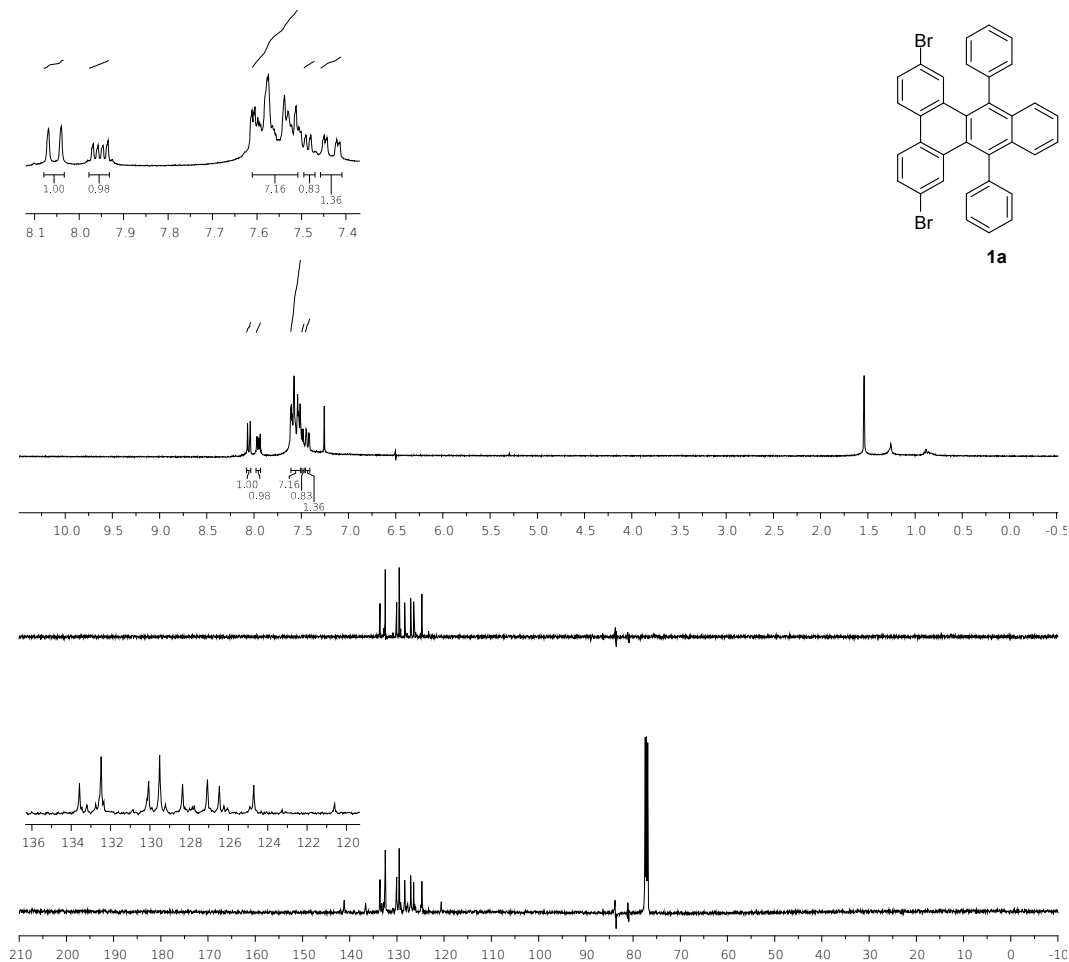


Figure 9:  $^1\text{H}$ , DEPT 135 and  $^{13}\text{C}$  NMR spectra of compound **1a**.

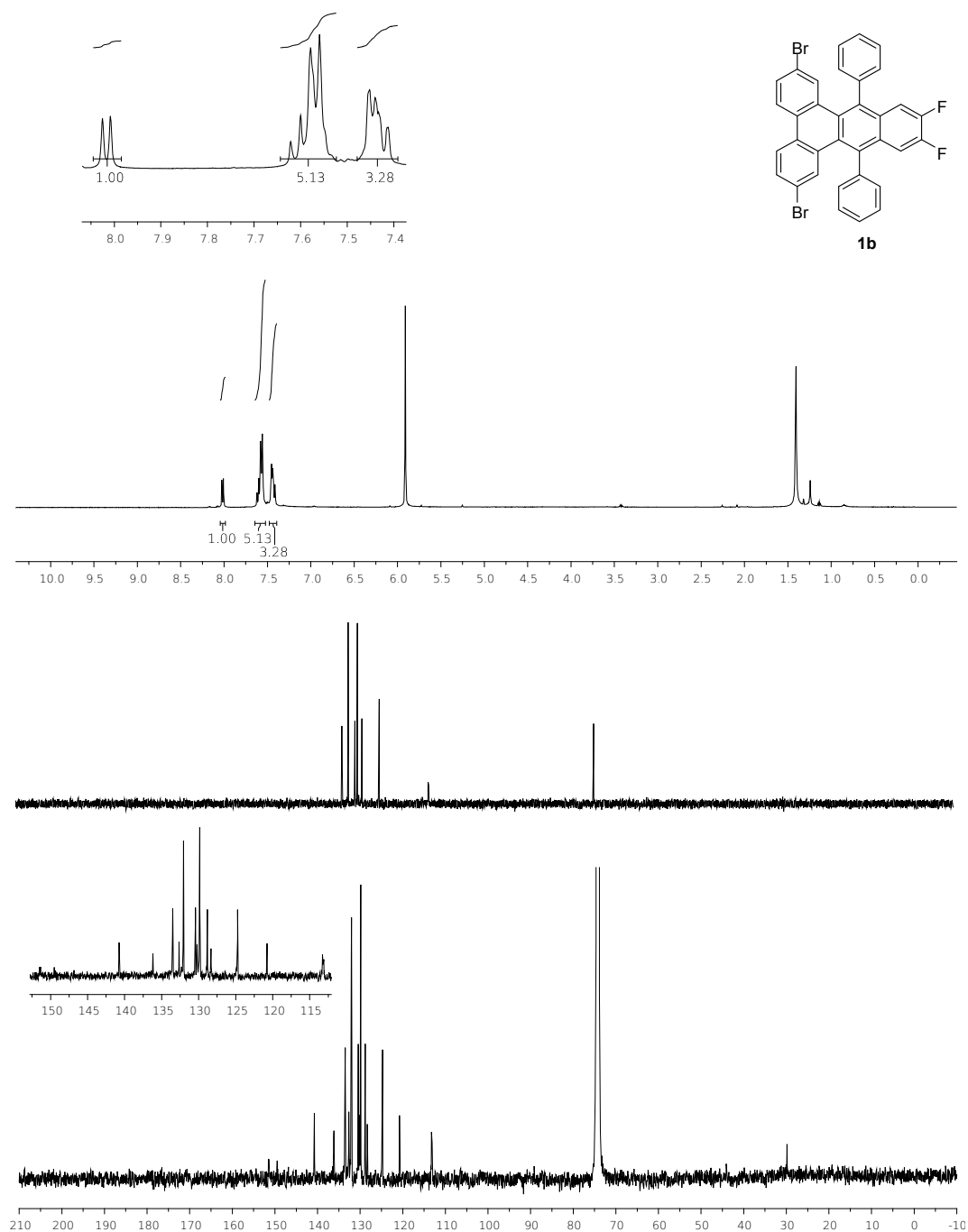


Figure 10:  $^1\text{H}$ , DEPT 135 and  $^{13}\text{C}$  NMR spectra of compound **1b**.

## References

1. Wagner, P.; Ewels, C. P.; Adjizian, J.-J.; Magaud, L.; Pochet, P.; Roche, S.; Lopez-Bezanilla, A.; Ivanovskaya, V. V.; Yaya, A.; Rayson, M. *et al.* Band Gap Engineering via Edge-Functionalization of Graphene Nanoribbons. *The Journal of Physical Chemistry C* **2013**, *117*, 26790–26796.
2. Tan, Y.-Z.; Yang, B.; Parvez, K.; Narita, A.; Osella, S.; Beljonne, D.; Feng, X.; Müllen, K. Atomically precise edge chlorination of nanographenes and its application in graphene nanoribbons. *Nature Communications* **2013**, *4*, 2646.
3. Ruffieux, P.; Wang, S.; Yang, B.; Sánchez-Sánchez, C.; Liu, J.; Dienel, T.; Talirz, L.; Shinde, P.; Pignedoli, C. A.; Passerone, D. *et al.* On-surface synthesis of graphene nanoribbons with zigzag edge topology. *Nature* **2016**, *531*, 489–492.
4. Carbonell-Sanromà, E.; Hieulle, J.; Vilas-Varela, M.; Brandimarte, P.; Iraola, M.; Baragán, A.; Li, J.; Abadia, M.; Corso, M.; Sánchez-Portal, D. *et al.* Doping of Graphene Nanoribbons *via* Functional Group Edge Modification. *ACS Nano* **2017**, *11*, 7355–7361.
5. Slota, M.; Keerthi, A.; Myers, W. K.; Tretyakov, E.; Baumgarten, M.; Ardavan, A.; Sadeghi, H.; Lambert, C. J.; Narita, A.; Müllen, K. *et al.* Magnetic edge states and coherent manipulation of graphene nanoribbons. *Nature* **2018**, *557*, 691–695.
6. Moreno, C.; Vilas-Varela, M.; Kretz, B.; Garcia-Lekue, A.; Costache, M. V.; Paradinas, M.; Panighel, M.; Ceballos, G.; Valenzuela, S. O.; Peña, D. *et al.* Bottom-up synthesis of multifunctional nanoporous graphene. *Science* **2018**, *360*, 199–203.
7. Shekhirev, M.; Zahl, P.; Sinitskii, A. Phenyl Functionalization of Atomically Precise Graphene Nanoribbons for Engineering Inter-ribbon Interactions and Graphene Nanopores. *ACS Nano* **2018**, *12*, 8662–8669.

8. Cho, K. M.; Cho, S.-Y.; Chong, S.; Koh, H.-J.; Kim, D. W.; Kim, J.; Jung, H.-T. Edge-Functionalized Graphene Nanoribbon Chemical Sensor: Comparison with Carbon Nanotube and Graphene. *ACS Applied Materials & Interfaces* **2018**, *10*, 42905–42914.
9. Joshi, D.; Hauser, M.; Veber, G.; Berl, A.; Xu, K.; Fischer, F. R. Super-Resolution Imaging of Clickable Graphene Nanoribbons Decorated with Fluorescent Dyes. *Journal of the American Chemical Society* **2018**, *140*, 9574–9580.
10. Moreno, C.; Paradinas, M.; Vilas-Varela, M.; Panighel, M.; Ceballos, G.; Peña, D.; Mugarza, A. On-surface synthesis of superlattice arrays of ultra-long graphene nanoribbons. *Chemical Communications* **2018**, *54*, 9402–9405.
11. Keerthi, A.; Radha, B.; Rizzo, D.; Lu, H.; Diez Cabanes, V.; Hou, I. C.-Y.; Beljonne, D.; Cornil, J.; Casiraghi, C.; Baumgarten, M. *et al.* Edge Functionalization of Structurally Defined Graphene Nanoribbons for Modulating the Self-Assembled Structures. *Journal of the American Chemical Society* **2017**, *139*, 16454–16457.
12. Franc, G.; Gourdon, A. Covalent networks through on-surface chemistry in ultra-high vacuum: state-of-the-art and recent developments. *Physical Chemistry Chemical Physics* **2011**, *13*, 14283.
13. On-Surface Synthesis II: Proceedings of the International Workshop On-Surface Synthesis, San Sebastián, 27-30 June 2016. **2016**,
14. Clair, S.; de Oteyza, D. G. Controlling a Chemical Coupling Reaction on a Surface: Tools and Strategies for On-Surface Synthesis. *Chemical Reviews* **2019**, *119*, 4717–4776.
15. Hayashi, H.; Yamaguchi, J.; Jippo, H.; Hayashi, R.; Aratani, N.; Ohfuchi, M.; Sato, S.; Yamada, H. Experimental and Theoretical Investigations of Surface-Assisted Graphene Nanoribbon Synthesis Featuring Carbon–Fluorine Bond Cleavage. *ACS Nano* **2017**, *11*, 6204–6210.



16. Cai, J.; Ruffieux, P.; Jaafar, R.; Bieri, M.; Braun, T.; Blankenburg, S.; Muoth, M.; Seitsonen, A. P.; Saleh, M.; Feng, X. *et al.* Atomically precise bottom-up fabrication of graphene nanoribbons. *Nature* **2010**, *466*, 470–473.
17. Basagni, A.; Sedona, F.; Pignedoli, C. A.; Cattelan, M.; Nicolas, L.; Casarin, M.; Sami, M. Molecules–Oligomers–Nanowires–Graphene Nanoribbons: A Bottom-Up Stepwise On-Surface Covalent Synthesis Preserving Long-Range Order. *Journal of the American Chemical Society* **2015**, *137*, 1802–1808.
18. Batra, A.; Cvetko, D.; Kladnik, G.; Adak, O.; Cardoso, C.; Ferretti, A.; Prezzi, D.; Molinari, E.; Morgante, A.; Venkataraman, L. Probing the mechanism for graphene nanoribbon formation on gold surfaces through X-ray spectroscopy. *Chem. Sci.* **2014**, *5*, 4419–4423.
19. Moreno, C.; Panighel, M.; Vilas-Varela, M.; Sauthier, G.; Tenorio, M.; Ceballos, G.; Peña, D.; Mugarza, A. Critical Role of Phenyl Substitution and Catalytic Substrate in the Surface-Assisted Polymerization of Dibromobianthracene Derivatives. *Chemistry of Materials* **2019**, *31*, 331–341.
20. Ohtomo, M.; Jippo, H.; Hayashi, H.; Yamaguchi, J.; Ohfuchi, M.; Yamada, H.; Sato, S. Interpolymer Self-Assembly of Bottom-up Graphene Nanoribbons Fabricated from Fluorinated Precursors. *ACS Applied Materials & Interfaces* **2018**, *10*, 31623–31630.
21. Blankenburg, S.; Cai, J.; Ruffieux, P.; Jaafar, R.; Passerone, D.; Feng, X.; Müllen, K.; Fasel, R.; Pignedoli, C. A. Intraribbon Heterojunction Formation in Ultranarrow Graphene Nanoribbons. *ACS Nano* **2012**, *6*, 2020–2025.
22. Bronner, C.; Stremlau, S.; Gille, M.; Brauße, F.; Haase, A.; Hecht, S.; Tegeder, P. Aligning the Band Gap of Graphene Nanoribbons by Monomer Doping. *Angewandte Chemie* **2013**, *125*, 4518–4521.

23. Cai, J.; Pignedoli, C. A.; Talirz, L.; Ruffieux, P.; Söde, H.; Liang, L.; Meunier, V.; Berger, R.; Li, R.; Feng, X. *et al.* Graphene nanoribbon heterojunctions. *Nature Nanotechnology* **2014**, *9*, 896–900.
24. Merino-Díez, N.; Garcia-Lekue, A.; Carbonell-Sanromà, E.; Li, J.; Corso, M.; Collazzo, L.; Sedona, F.; Sánchez-Portal, D.; Pascual, J. I.; de Oteyza, D. G. Width-Dependent Band Gap in Armchair Graphene Nanoribbons Reveals Fermi Level Pinning on Au(111). *ACS Nano* **2017**, *11*, 11661–11668.
25. Yang, L.; Park, C.-H.; Son, Y.-W.; Cohen, M. L.; Louie, S. G. Quasiparticle Energies and Band Gaps in Graphene Nanoribbons. *Physical Review Letters* **2007**, *99*, 186801.
26. Nečas, D.; Klapetek, P. Gwyddion: an open-source software for SPM data analysis. *Open Physics* **2012**, *10*.
27. Artacho, E.; Sánchez-Portal, D.; Ordejón, P.; García, A.; Soler, J. M. Linear-Scaling ab-initio Calculations for Large and Complex Systems. *physica status solidi (b)* **1999**, *215*, 809–817.
28. Soler, J. M.; Artacho, E.; Gale, J. D.; García, A.; Junquera, J.; Ordejón, P.; Sánchez-Portal, D. The SIESTA method for ab initio order-N materials simulation. *Journal of Physics: Condensed Matter* **2002**, *14*, 2745–2779.
29. García-Gil, S.; García, A.; Lorente, N.; Ordejón, P. Optimal strictly localized basis sets for noble metal surfaces. *Physical Review B* **2009**, *79*, 075441.
30. Gonzalez-Lakunza, N.; Fernández-Torrente, I.; Franke, K. J.; Lorente, N.; Arnau, A.; Pascual, J. I. Formation of Dispersive Hybrid Bands at an Organic-Metal Interface. *Physical Review Letters* **2008**, *100*, 156805.
31. Troullier, N.; Martins, J. L. Efficient pseudopotentials for plane-wave calculations. *Physical Review B* **1991**, *43*, 1993–2006.

1  
2  
3  
4  
5  
6  
7  
8  
9  
10  
11  
12  
13  
14  
15  
16  
17  
18  
19  
20  
21  
22  
23  
24  
25  
26  
27  
28  
29  
30  
31  
32  
33  
34  
35  
36  
37  
38  
39  
40  
41  
42  
43  
44  
45  
46  
47  
48  
49  
50  
51  
52  
53  
54  
55  
56  
57  
58  
59  
60

32. Dion, M.; Rydberg, H.; Schröder, E.; Langreth, D. C.; Lundqvist, B. I. Van der Waals Density Functional for General Geometries. *Physical Review Letters* **2004**, *92*, 599–610.

33. Klimeš, J.; Bowler, D. R.; Michaelides, A. Chemical accuracy for the van der Waals density functional. *Journal of Physics: Condensed Matter* **2010**, *22*, 022201.

34. Zuzak, R.; Castro-Esteban, J.; Brandimarte, P.; Englund, M.; Cobas, A.; Piątkowski, P.; Kolmer, M.; Pérez, D.; Guitián, E.; Szymonski, M. *et al.* Building a 22-ring nanographene by combining in-solution and on-surface syntheses. *Chemical Communications* **2018**, *54*, 10256–10259.

## Graphical TOC Entry

